

# Efficient waveguide-coupling of metal-clad nanolaser cavities

Myung-Ki Kim, Amit M. Lakhani, and Ming C. Wu\*

Department of Electrical Engineering and Computer Sciences, University of California, Berkeley, CA 94720, USA  
wu@eecs.berkeley.edu

**Abstract:** Many remarkable semiconductor-based nanolaser cavities using metal have been reported in past few years. However, the efficient coupling of these small cavities to waveguides still remains a large challenge. Here, we show highly efficient coupling of a semiconductor-based metal-clad nanolaser cavity operating in the fundamental dielectric cavity mode to a silicon-on-insulator waveguide. By engineering the effective refractive index and the field distribution of the cavity mode, a coupling efficiency as high as 78% can be achieved for a metal-clad nanolaser with a modal volume of  $0.28 (\lambda/n)^3$  while maintaining a high optical quality factor of  $> 600$ .

©2011 Optical Society of America

OCIS codes: (250.5960) Semiconductor lasers; (250.5300) Photonic integrated circuits.

---

## References and links

1. M. T. Hill, Y.-S. Oei, B. Smalbrugge, Y. Zhu, T. de Vries, P. J. van Veldhoven, F. W. M. van Otten, T. J. Eijkemans, J. P. Turkiewicz, H. de Waardt, E. J. Geluk, S.-H. Kwon, Y.-H. Lee, R. Notzel, and M. K. Smit, "Lasing in metallic-coated nanocavities," *Nat. Photonics* **1**(10), 589–594 (2007).
2. M. T. Hill, M. Marell, E. S. P. Leong, B. Smalbrugge, Y. Zhu, M. Sun, P. J. van Veldhoven, E. J. Geluk, F. Karouta, Y.-S. Oei, R. Nötzel, C.-Z. Ning, and M. K. Smit, "Lasing in metal-insulator-metal sub-wavelength plasmonic waveguides," *Opt. Express* **17**(13), 11107–11112 (2009).
3. M. A. Noginov, G. Zhu, A. M. Belgrave, R. Bakker, V. M. Shalaev, E. E. Narimanov, S. Stout, E. Herz, T. Suteewong, and U. Wiesner, "Demonstration of a spaser-based nanolaser," *Nature* **460**(7259), 1110–1112 (2009).
4. R. F. Oulton, V. J. Sorger, T. Zentgraf, R.-M. Ma, C. Gladden, L. Dai, G. Bartal, and X. Zhang, "Plasmon lasers at deep subwavelength scale," *Nature* **461**(7264), 629–632 (2009).
5. K. Yu, A. Lakhani, and M. C. Wu, "Subwavelength metal-optic semiconductor nanopatch lasers," *Opt. Express* **18**(9), 8790–8799 (2010).
6. M. P. Nezhad, A. Simic, O. Bondarenko, B. Slutsky, A. Mizrahi, L. Feng, V. Lomakin, and Y. Fainman, "Room-temperature subwavelength metallo-dielectric lasers," *Nat. Photonics* **4**(6), 395–399 (2010).
7. C.-Y. Lu, S.-W. Chang, S. L. Chuang, T. D. Germann, and D. Bimberg, "Metal-cavity surface-emitting microlaser at room temperature," *Appl. Phys. Lett.* **96**(25), 251101 (2010).
8. S.-H. Kwon, J.-H. Kang, C. Seassal, S.-K. Kim, P. Regreny, Y.-H. Lee, C. M. Lieber, and H.-G. Park, "Subwavelength plasmonic lasing from a semiconductor nanodisk with silver nanopatch cavity," *Nano Lett.* **10**(9), 3679–3683 (2010).
9. A. M. Lakhani, K. Yu, and M. C. Wu, "Lasing in subwavelength semiconductor nanopatches," *Semicond. Sci. Technol.* **26**(1), 014013 (2011).
10. R.-M. Ma, R. F. Oulton, V. J. Sorger, G. Bartal, and X. Zhang, "Room-temperature sub-diffraction-limited plasmon laser by total internal reflection," *Nat. Mater.* **10**(2), 110–113 (2011).
11. K. Ding, Z. Liu, L. Yin, H. Wang, R. Liu, M. T. Hill, M. J. H. Marell, P. J. van Veldhoven, R. Nötzel, and C. Z. Ning, "Electrical injection, continuous wave operation of subwavelength-metallic-cavity lasers at 260 K," *Appl. Phys. Lett.* **98**(23), 231108 (2011).
12. M.-K. Kim, S. H. Lee, M. Choi, B.-H. Ahn, N. Park, Y.-H. Lee, and B. Min, "Low-loss surface-plasmonic nanobeam cavities," *Opt. Express* **18**(11), 11089–11096 (2010).
13. Q. Ding, A. Mizrahi, Y. Fainman, and V. Lomakin, "Dielectric shielded nanoscale patch laser resonators," *Opt. Lett.* **36**(10), 1812–1814 (2011).
14. S. L. McCall, A. F. J. Levi, R. E. Slusher, S. J. Pearton, and R. A. Logan, "Whispering-gallery mode microdisk lasers," *Appl. Phys. Lett.* **60**(3), 289 (1992).
15. J. C. Johnson, H.-J. Choi, K. P. Knutsen, R. D. Schaller, P. Yang, and R. J. Saykally, "Single gallium nitride nanowire lasers," *Nat. Mater.* **1**(2), 106–110 (2002).
16. Z. Zhang, L. Yang, V. Liu, T. Hong, K. Vahala, and A. Scherer, "Visible submicron microdisk lasers," *Appl. Phys. Lett.* **90**(11), 111119 (2007).

17. S. Reitzenstein, T. Heindel, C. Kistner, A. Rahimi-Iman, C. Schneider, S. Hofling, and A. Forchel, "Low threshold electrically pumped quantum dot-micropillar lasers," *Appl. Phys. Lett.* **93**(6), 061104 (2008).
18. A. W. Fang, H. Park, O. Cohen, R. Jones, M. J. Paniccia, and J. E. Bowers, "Electrically pumped hybrid AlGaInAs-silicon evanescent laser," *Opt. Express* **14**(20), 9203–9210 (2006).
19. J. Van Campenhout, P. Rojo Romeo, P. Regreny, C. Seassal, D. Van Thourhout, S. Verstuyft, L. Di Cioccio, J.-M. Fedeli, C. Lagahe, and R. Baets, "Electrically pumped InP-based microdisk lasers integrated with a nanophotonic silicon-on-insulator waveguide circuit," *Opt. Express* **15**(11), 6744–6749 (2007).
20. D. Liang, M. Fiorentino, T. Okumura, H.-H. Chang, D. T. Spencer, Y.-H. Kuo, A. W. Fang, D. Dai, R. G. Beausoleil, and J. E. Bowers, "Electrically-pumped compact hybrid silicon microring lasers for optical interconnects," *Opt. Express* **17**(22), 20355–20364 (2009).
21. J. Van Campenhout, P. R. A. Binetti, P. Rojo Romeo, and P. Regreny, C. Seassal, X. J. M. Leijtens, T. de Vries, Y. S. Oei, P. J. van Veldhoven, R. N'otzel, L. Di Cioccio, J.-M. Fedeli, M. K. Smit, D. Van Thourhout, and R. Baets, "Low-footprint optical interconnect on an SOI chip through heterogeneous integration of InP-based microdisk lasers and microdetectors," *IEEE Photon. Technol. Lett.* **21**(8), 522–524 (2009).
22. G. Roelkens, L. Liu, D. Liang, R. Jones, A. W. Fang, B. Koch, and J. E. Bowers, "III-V/silicon photonics for on-chip and intra-chip optical interconnects," *Laser Photon. Rev.* **4**(6), 751–779 (2010).
23. L. C. Kimerling, D. Ahn, A. B. Apsel, M. Beals, D. Carothers, Y.-K. Chen, T. Conway, D. M. Gill, M. Grove, C.-Y. Hong, M. Lipson, J. Liu, J. Michel, D. Pan, S. S. Patel, A. T. Pomerene, M. Rasras, D. K. Sparacin, K.-Y. Tu, A. E. White, and C. W. Wong, "Electronic-photonic integrated circuits on the CMOS platform," *Proc. SPIE* **6125**, 612502, 612502-10 (2006).
24. J. S. Orcutt, A. Khilo, M. A. Popovic, C. W. Holzwarth, B. Moss, H. Li, M. S. Dahlem, T. D. Bonifield, F. X. Kaertner, E. P. Ippen, J. L. Hoyt, R. J. Ram, and V. Stojanovic, "Demonstration of an Electronic Photonic Integrated Circuit in a Commercial Scaled Bulk CMOS Process," *Proc. Conf. Lasers and Electro-Optics (CLEO), Optical Soc. of America* (2008).
25. A. V. Krishnamoorthy and K. W. Goossen, "Optoelectronic-VLSI: Photonics integrated with VLSI circuits," *IEEE J. Sel. Top. Quantum Electron.* **4**(6), 899–912 (1998).
26. P. B. Johnson and R. W. Christy, "Optical Constants of the Noble Metals," *Phys. Rev. B* **6**(12), 4370–4379 (1972).

---

## 1. Introduction

In the past few years, the laser community has made significant progress in designing and building metal optic nanocavities [1–13]. Such cavities make it possible to achieve subwavelength lasers without excessive radiation losses [14–17]. Subwavelength lasers have become very attractive as an enabler of nanophotonic integrated circuits due to their small size and low energy consumption. Yet, the radiation patterns of nanolasers (particularly the fundamental and other lower-order modes) tend to be very broad, making it difficult to couple the output light efficiently into integrated waveguides. Coupling light from these nanocavities to single mode silicon-on-insulator (SOI) waveguides is particularly interesting because it provides a means to integrate laser sources for silicon photonics technology [18–25]. Recently, Ding et al. have proposed dielectric shielded patch lasers that couple to III-V waveguides with 22% efficiency [13]. Yet, the lossy III-V waveguides are constructed on a lossy metal substrate, making integration with silicon-on-insulator photonics much more difficult.

In this paper, we introduce a metal-clad nanolaser directly integrated on top of a silicon waveguide. We systematically engineer the electromagnetic mode profile of the nanocavity to optimize the external efficiency of the laser into a silicon waveguide while maintaining a high quality factor. By altering the distribution of the in-plane wavevectors ( $k$ ) of the cavity mode, we are able to achieve coupling efficiencies as high as 78% while maintaining mode volumes of  $0.28 (\lambda/n)^3$  and quality factors  $> 600$ . We believe this compact and highly efficient device provides a very powerful platform for integration of III-V devices on silicon and enables a full complement of ultra-compact optical communication devices from lasers and amplifiers to modulators and detectors.

## 2. High-Q metal-clad nanocavity

In Fig. 1, we schematically present our proposed metal-clad nanolaser integrated onto a Si waveguide. The actual electromagnetic nanocavity consists of an InGaAsP bulk semiconductor cuboid with a height ( $h$ ) of 350 nm, a width ( $w$ ) of 350 nm, and a variable length ( $l$ ). The device is also configured for electrical carrier injection by introducing doped InP posts on the top and bottom of the cavity. To reduce the resistivity of the laser diode, 50

$nm$  thin doped InGaAsP pads are used as the ohmic contacts to the n- and p-metal layers. The n-InGaAsP electrode has the same length and width as the InGaAsP nanocavity ( $l$  by  $350\text{ nm}$ ). For the cubic cavity structure with  $l = 350\text{ nm}$ , the cavity operates in the fundamental transverse electric (TE) mode that resembles a donut at a frequency of  $204.8\text{ THz}$  ( $1.46\text{ }\mu\text{m}$ ). The second mode is spectrally separated from the first mode by  $44\text{ THz}$  ( $258\text{ nm}$ ). An  $\text{SiO}_2$  cladding also envelops the device with a certain thickness that can be engineered to control the quality factor ( $Q$ ) of the cavity and achieve the highest coupling rate into the Si-waveguide. Finally, to suppress unwanted radiation, we coat the entire cavity with  $100\text{ nm}$  of silver [26] (except on the bottom). The width of the Si-waveguide is designed to be the same as the cavity in order to simplify the fabrication process so that the nanolaser and waveguide are self-aligned, as shown in Fig. 1c. We also fix the thickness of the waveguide to  $120\text{ nm}$  to guarantee that it operates in the single-mode regime. Finally, we use a  $50\text{ nm}$  interfacial  $\text{SiO}_2$  layer between the p-InGaAsP and Si-waveguide in a molecular wafer bonding process [22], as shown in Fig. 1b.

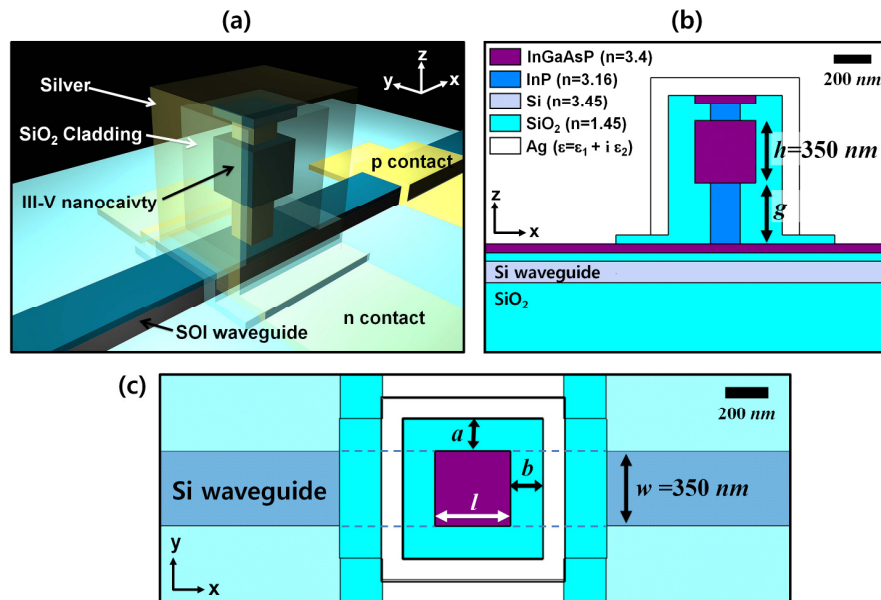


Fig. 1. Perspective (a) and cross-sectional (b, c) schematic views of a Si-waveguide coupled metal-clad nanolaser cavity. Here, the nanolaser cavity is designed as a cuboid structure with a height ( $h$ ) of  $350\text{ nm}$ , a width ( $w$ ) of  $350\text{ nm}$ , and a variable length ( $l$ ).

Initially, we focus on optimizing the nanolaser without the Si-waveguide. The first parameter we engineer is the thickness of the  $\text{SiO}_2$  cladding by simulating the cavity structures using finite-difference time-domain (FDTD) simulations. To study the effects of the cladding, we first place the nanolaser cavity on a pure silicon substrate instead of a Si-waveguide (Fig. 2a) to avoid any second-order effects that may result due to variations in coupling efficiency as a function of cladding thickness. We also keep the cladding thickness the same in both x- and y-directions ( $a = b$ , where  $a$  and  $b$  are defined in Fig. 1c) to preserve the symmetry of the cavity mode. The heights of top and bottom InP posts are initially fixed at  $100\text{ nm}$  and  $600\text{ nm}$ , respectively, and we find that the InP posts must be undercut by at least  $90\text{ nm}$  to maintain a high quality factor nanocavity. Here, the cavity length ( $l$ ) is fixed at  $350\text{ nm}$ . In Fig. 2b, we can see that the  $Q$ -factor of the device depends sensitively on the  $\text{SiO}_2$  thickness. If the  $\text{SiO}_2$  is  $150\text{ nm}$  thick, we are able to achieve a maximum  $Q$ -factor of 1700. This optimal cladding thickness suggests that there is a trade-off between metal and radiation loss. If we decompose the total cavity quality factor into radiation ( $Q_{rad}$ ) and the absorption ( $Q_{abs}$ ) with the relation of  $Q_{total}^{-1} = Q_{rad}^{-1} + Q_{abs}^{-1}$  (Fig. 2c), we find that for cladding thicknesses

larger than 225 nm, radiation is the dominant loss mechanism in the cavity. Such large amounts of radiation are the result of the low effective refractive index of the fundamental mode resulting in weak vertical confinement. To investigate the effect of cladding size on radiation, we transform the spatial modes of two cavities with cladding thicknesses of 300 nm and 150 nm, respectively seen in Figs. 3a and 3b, into the Fourier domain to see the in-plane wavevector distribution ( $k_{||}$ ) of the cavity modes (Figs. 3e and 3f). Here, the  $k$ -components inside the white dotted line of  $n = 1.5$  represent the vertical radiation components of the mode into the SiO<sub>2</sub> cladding since they fail to satisfy the condition of total-internal-reflection (TIR) along the vertical direction. In comparing the two different cavities, we see that the device with a cladding of 300 nm has much more energy that fails to satisfy TIR compared to the more thinly clad device. From the effective index viewpoint, the device with 300 nm cladding has an effective index of  $n = 1.63$  while the cavity with 150 nm of SiO<sub>2</sub> has an effective index of  $n = 2.0$ . Thus, we see that although thicker claddings result in less metal loss, the effective index of the mode decreases, resulting in large amounts of radiation. Specifically, a cladding of 300 nm around the nanocavity results in a radiation to total loss ratio of 84%. We can achieve a radiation to total loss ratio of 50% when the cladding is ~225 nm thick. Although we can achieve high suppression of radiation by reducing the cladding thickness, the absorption loss from the metal reflector starts to become significant. As a result, the maximum total quality factor is the result of the trade-off between these two loss channels, as shown in Fig. 2c.

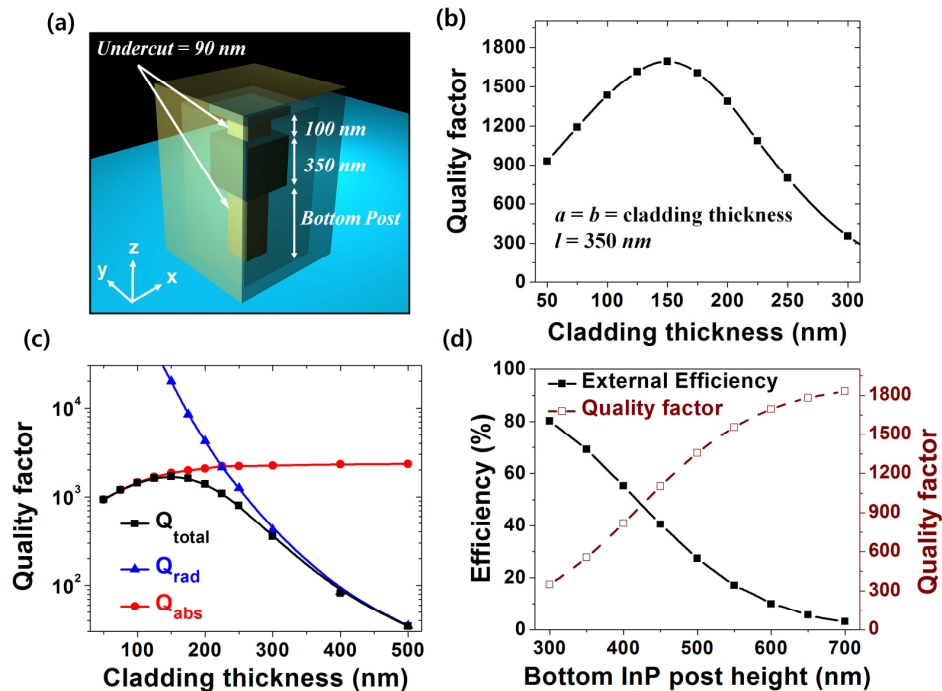


Fig. 2. (a) Schematic of a metal-clad nanocavity on a semiconductor substrate. (b) Quality factor as a function of the cladding size ( $a = b$ ). (c) Total  $Q$ -factor, radiation  $Q$ -factor, and absorption  $Q$ -factor as a function of cladding size. (d) External efficiency and quality factor of the cavity as a function of bottom InP post height between the nanocavity and the substrate.

After optimizing the SiO<sub>2</sub> cladding to obtain a quality factor > 1700, the bottom InP post height can also be engineered to create high total external efficiency (defined to be the ratio of total radiated power and total lost power, including metal loss). In Fig. 2d, we show the dependence of the cavity quality factor as well as the external efficiency of the cavity as a function of bottom InP post height. As we reduce the post height, the radiation rate increases

due to strong coupling of the cavity mode with the continuum modes of the high-index substrate. Thus, the external efficiency can be engineered from 10% to 55% by reducing the bottom post height from 600 nm to 400 nm although total  $Q$ -factor is reduced from 1700 to 810.

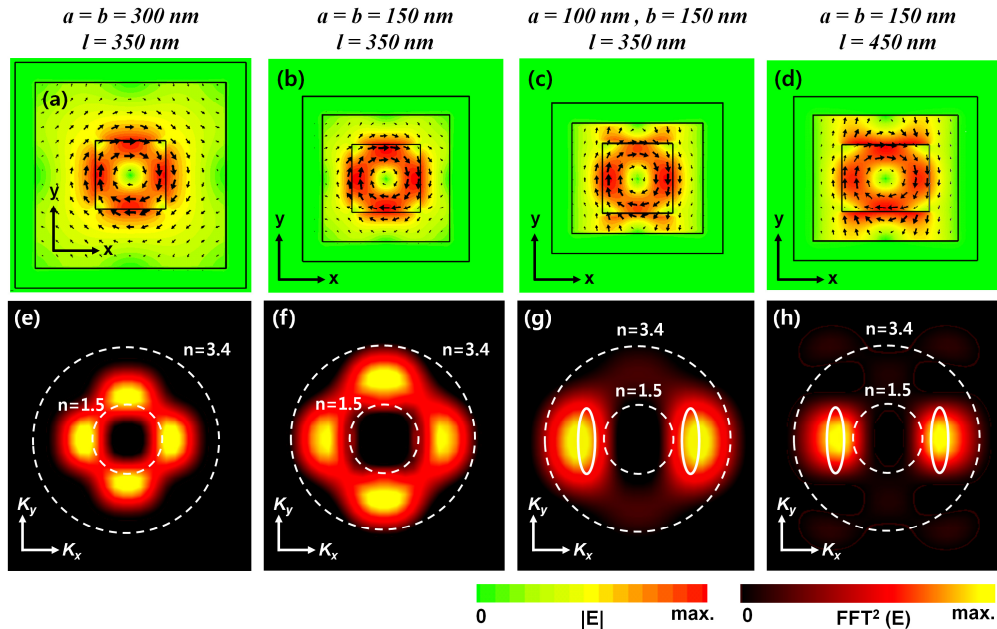


Fig. 3. Electric field intensity profile (vector plot overlaid) and the Fourier transform of the electric field profile for (a, e)  $a = b = 300 \text{ nm}$  and  $l = 350 \text{ nm}$ , (b, f)  $a = b = 150 \text{ nm}$  and  $l = 350 \text{ nm}$  (c, g)  $a = 100 \text{ nm}$ ,  $b = 150 \text{ nm}$  and  $l = 350 \text{ nm}$ , and (d, h)  $a = b = 150 \text{ nm}$  and  $l = 450 \text{ nm}$ , respectively. Here,  $a$ ,  $b$  and  $l$  are defined in Fig. 1c. The closed solid lines in (g) and (h) enclose the wavevectors that couple to the Si-waveguide.

### 3. High coupling to Si-waveguide

After optimizing the cavity design to have a high quality factor and a high external efficiency, we focus our attention to efficiently coupling the device to a conventional waveguide. Thus, we aim to maximize the efficiency of coupling of laser radiation into the Si-waveguide ( $\gamma_{\text{coupling}}/\gamma_{\text{rad}}$ ). Here,  $\gamma_{\text{coupling}}$  and  $\gamma_{\text{rad}}$  represent the cavity-to-waveguide coupling rate and the total cavity radiation rate, respectively, as seen in Fig. 4a. The emission pattern of the nanocavity is naturally divergent due its small size, making it difficult to couple the output light efficiently into a waveguide. Among various coupling approaches, coupling light to a single mode SOI waveguide is particularly interesting because it provides a means to integrate laser sources for silicon photonics technology. Using wafer bonding techniques, the metal-clad nanocavity can be integrated onto a Si-waveguide [18–20]. The light from the nanocavity will then couple to the waveguide via weak evanescent coupling from the bottom of the nanocavity. For example, a nanocavity with a cladding thickness and bottom post height ( $g$ ) of 150 nm ( $a = b = 150 \text{ nm}$ ) and 600 nm, respectively, has a 22% coupling efficiency to the Si-waveguide. To further couple light into the waveguide, we modify the field distribution of the cavity mode to break the symmetry of the cavity mode and make it preferentially radiate in the  $x$ -direction into the waveguide. There are two main ways to break the symmetry of the nanocavity: we can introduce asymmetry in the cladding thickness in the  $x$ - and  $y$ -directions around a cubic cavity, as shown in Fig. 3c, or we can modify the cubic InGaAsP gain region to make it rectangular, as shown in Fig. 3d. We investigate both cases.

In Fig. 3c, we show the electric-field distribution of a device with asymmetric cladding thicknesses along the  $x$ - and  $y$ -direction with  $a = 100 \text{ nm}$  and  $b = 150 \text{ nm}$ . As we might

expect, the symmetry of the field-profile is reduced and the electric field vectors point predominantly along the y-direction (when  $a < b$ ). Accordingly, the in-plane  $k$ -components in the Fourier domain are highly concentrated on the  $k_x$  axis, as shown in Fig. 3g. Thus, by making the cladding asymmetric, we can independently engineer the amount of metallic reflection on the cavity mode along the x- and y-direction.

Similarly, we can modify the InGaAsP cavity to make it rectangular while keeping the cladding thickness the same. In this case, the electric field vectors again point predominantly along the y-direction when  $l > 350$  nm, as shown in Fig. 3d. Accordingly, the in-plane  $k$ -components in the Fourier domain are highly concentrated on the  $k_x$  axis as well, as shown in Fig. 3h. The closed solid white lines in Figs. 3h and f enclose the approximate wavevectors that couple to the Si-waveguide. Since the in-plane wavevectors of the cavity and the waveguide modes are largely overlapped, we verify the high coupling rate from the nanocavity to the waveguide.

In Fig. 4, we summarize the influence of various design parameters on the coupling efficiency, energy confinement factor, cavity quality factor, and laser threshold gain. In Fig. 4b, we show how the coupling efficiency and energy confinement factor (in the III-V active region) change as a function of the y-cladding thickness ( $a$ ) for a fixed x-cladding thickness ( $b$ ), cavity length ( $l$ ), and bottom post height ( $g$ ) of 150 nm, 350 nm, and 600 nm, respectively. As we reduce  $a$  to less than 60 nm, the coupling efficiency to the Si-waveguide dramatically increases to over 75% although the confinement and quality factors are degraded as more field leaks out into the cladding and metal as  $a$  is reduced. Figure 4c shows the quality factor and threshold material gain coefficient for lasing as a function of  $a$ . Thus, if  $a$  is designed to be 60 nm, then the coupling efficiency is 76%, the threshold gain is 100 cm<sup>-1</sup>, and the cavity quality factor is ~1000.

If we make the InGaAsP cavity rectangular (we vary  $l$ ), then there is a potential advantage in fabrication, since the oxide can be kept uniformly thick around the device. A rectangular cavity can also be self-aligned, making fabrication easier. Thus, if  $a = b = 150$  nm, and the bottom InP post height ( $g$ ) is kept at 600 nm, then a maximum coupling efficiency of 61% is achieved when  $l = 430$  nm (Fig. 4d). The confinement factor remains high at 79%, and the quality factor and threshold gain are 1440 and 62 cm<sup>-1</sup>, respectively (Fig. 4e). Thus, we obtain a smaller coupling efficiency for a cavity where we engineer  $l$  versus  $a$ . We attribute the smaller coupling efficiency to the fact that a 150 nm cladding thickness generates a lot of radiation into the substrate regardless of the shape of the nanocavity. Thus, there seems to be a tradeoff between coupling efficiency and ease of fabrication.

So far, even though we have optimized the coupling efficiency ( $\gamma_{coupling}/\gamma_{rad}$ ) of the nanocavity to the waveguide using two different methods, the total external efficiency ( $\gamma_{rad}/\gamma_{total}$ ) of the device remains low around 4% due to high metal loss. Here,  $\gamma_{total}$  represents the total energy decay rate in the cavity due to both metal and radiation loss, as shown in Fig. 4a. As before, however, we can engineer the external efficiency of our device by changing the height of the bottom InP post ( $g$ ), as shown in Fig. 4f. Here, we use asymmetric cladding to optimize our coupling efficiency by setting  $a$ ,  $b$ , and  $l$  to 60 nm, 150 nm and 350 nm, respectively. Interestingly, the coupling efficiency remains almost constant around 75% even if we change  $g$  from 200 ~700 nm. Thus, we can independently engineer coupling and total external efficiencies by tuning cladding asymmetry and bottom InP post height, respectively. However, the total quality factor is decreased as  $g$  is reduced since we increase our total radiation rate, as shown in Fig. 4g. Accordingly, the threshold III-V material gain for lasing is also increased.

After fully and systematically optimizing our nanolaser, we find that the device operates most efficiently when  $g$  and  $a$  are 350 nm and 60 nm, respectively, in a cubic cavity ( $l = 350$  nm). These dimensions result in high external efficiency and high  $Q$ -factor cavities. At these conditions, the coupling efficiency, the total external efficiency, the  $Q$ -factor, and the threshold material gain coefficient for lasing are calculated to be 78%, 43%, 630 and 153 cm<sup>-1</sup>, respectively

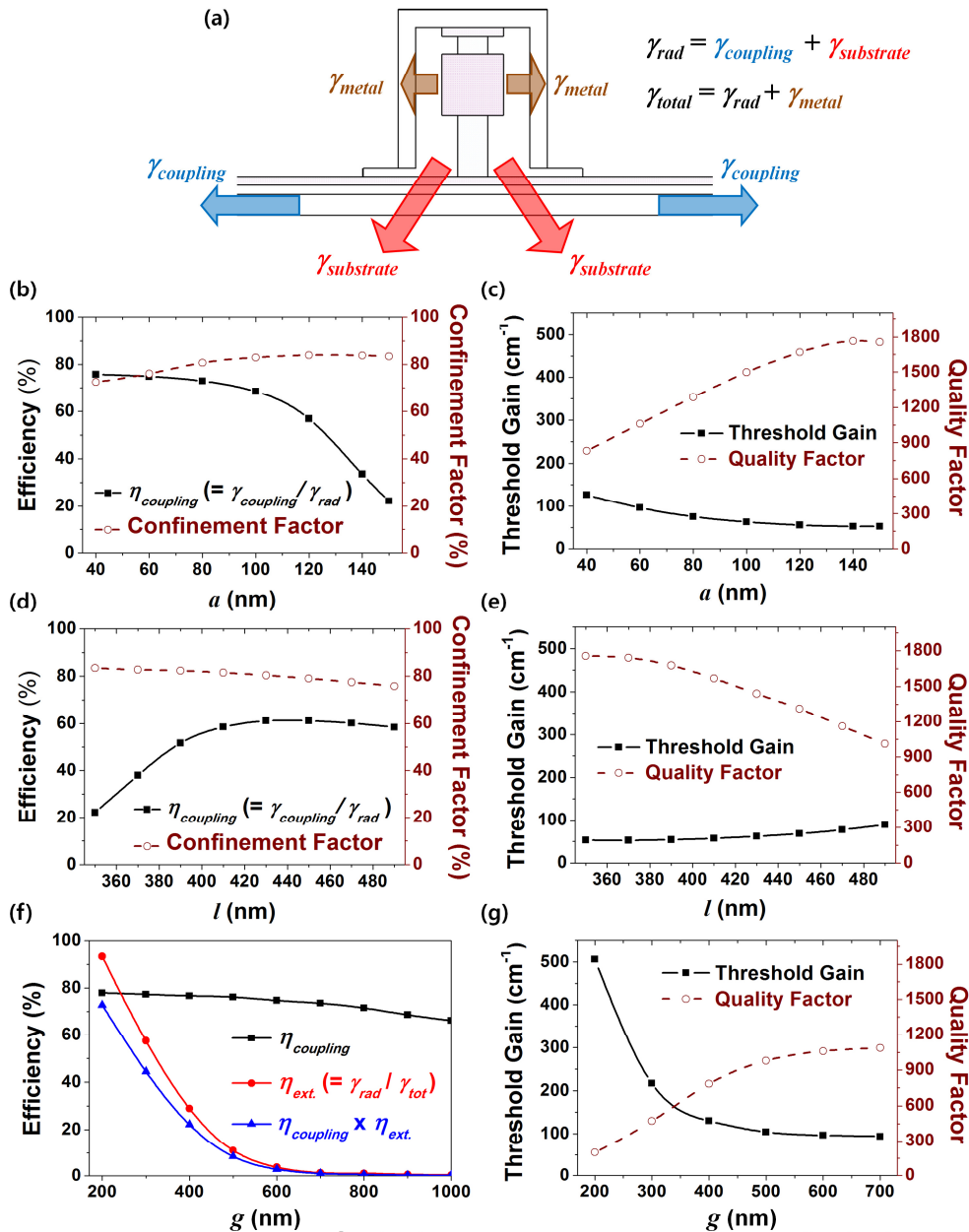


Fig. 4. (a) Illustration showing the various energy loss paths from the cavity including metal and radiation losses. (b, c, d, e) Coupling efficiency ( $\gamma_{coupling}/\gamma_{rad}$ ) to Si-waveguide, energy confinement factor into active region, threshold material gain coefficient for lasing, and cavity quality factor as a function of  $a$  and  $l$ , respectively, with  $b = 150 \text{ nm}$  and  $g = 600 \text{ nm}$ . (f, g) Coupling efficiency, total external efficiency, total energy efficiency to Si-waveguide, threshold material gain coefficient for lasing, and quality factor as a function of  $g$  for the optimal structure with  $a = 60 \text{ nm}$ ,  $b = 150 \text{ nm}$  and  $l = 350 \text{ nm}$ .

In Figs. 5a and b, we show the electric-field amplitudes in the same logarithm scale with 40 dB range for  $a = 60 \text{ nm}$ ,  $b = 150 \text{ nm}$ , and  $g = 350 \text{ nm}$ . These plots illustrate how much more efficiently the nanocavity functions when the y-cladding thickness is 60 nm versus 150

*nm*. The far-field radiation patterns to the substrate direction of these two cases, as seen in Figs. 5c and d, more clearly demonstrate how much the radiation is enhanced to the waveguide direction by the asymmetric claddings.

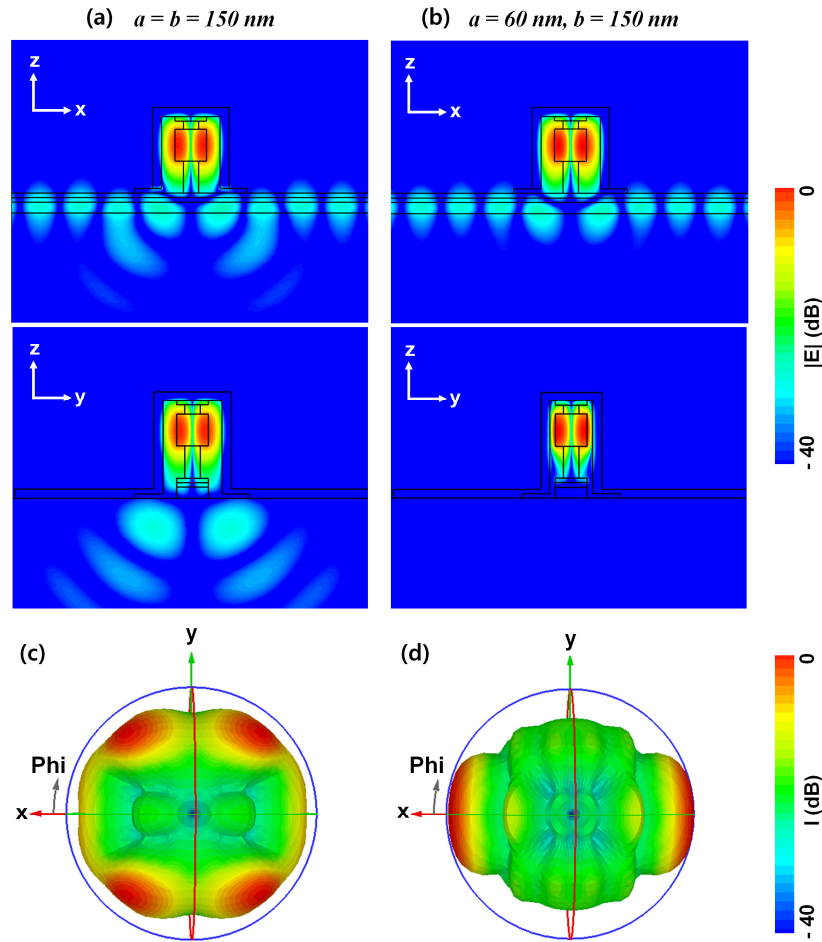


Fig. 5. Cross-sectional side views of  $|E|$  in logarithm scale with 40 dB range in the  $x-z$  and  $y-z$  planes for  $a$  of (a) 150 nm and (b) 60 nm, respectively, where  $b$  and  $g$  are fixed at 150 nm and 350 nm, respectively. Far-field radiation patterns to the substrate direction for  $a$  of (c) 150 nm and (d) 60 nm, respectively.

Finally, we have also explored the sensitivity of our design to various alignment errors that might occur in fabrication. In Fig. 6, we explore how the coupling efficiency and quality factor change when the  $\text{SiO}_2$  cladding is misaligned to the InGaAsP nanocavity in both  $x$ - and  $y$ -directions. Here, the parameters  $a$ ,  $b$ ,  $l$  and  $g$  are fixed at the optimized values of 60 nm, 150 nm, 350 nm and 350 nm, respectively. Since the field is stronger in this cavity mode in the  $y$ -direction due to thin 60 nm cladding, the coupling efficiency and quality factor are highly sensitive to misalignment in this direction, as shown in Fig. 6b. When the  $x$ - and  $y$ -shifts are larger than 90 nm and 37 nm, the coupling efficiency and Q-factor are degraded to less than 50% and 450, respectively.

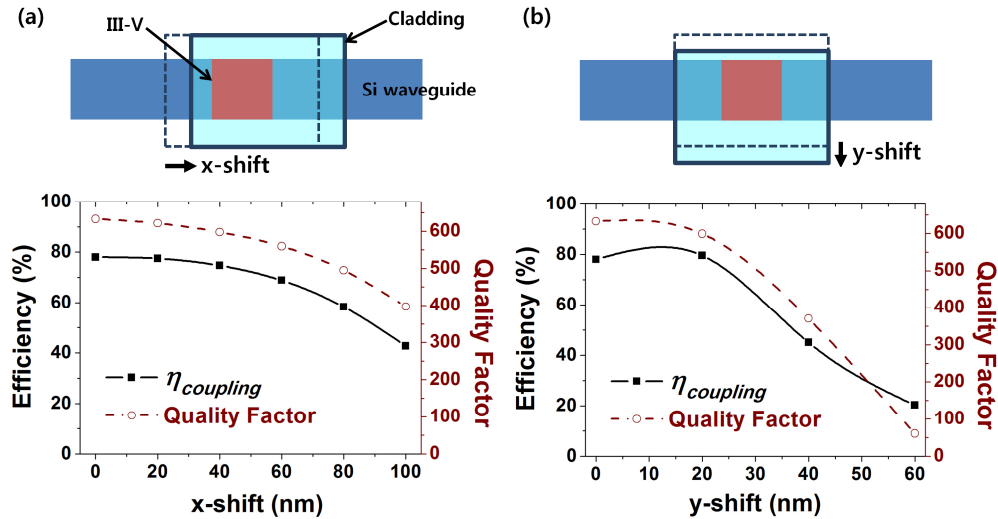


Fig. 6. Coupling efficiency and quality factor for nanocavities with misaligned cladding positions along the (a) x- and (b) y-direction.

#### 4. Conclusion

In conclusion, we have systematically studied a high  $Q$ -factor metal-clad semiconductor nanolaser with a footprint smaller than one wavelength that can be efficiently coupled to a Si-waveguide. By controlling the  $\text{SiO}_2$  cladding thickness in both x- and y-directions, we can engineer the effective refractive index of the cavity mode and obtain quality factors as high as 1700 with a modal volume of  $0.28 (\lambda/n)^3$ . When we introduce a Si-waveguide and engineer the field distribution of the cavity mode with asymmetric cladding thicknesses along x- and y-direction, the coupling efficiency can be highly enhanced to  $> 75\%$  while maintaining a high optical quality factor of  $> 1000$ . Finally, by engineering the bottom InP post height, we can also control the total external efficiency of the device. We believe this compact and highly efficient device provides a very powerful platform for integration of III-V devices on silicon, enabling a full complement of ultra-compact optical communication devices from lasers and amplifiers to modulators and detectors.

#### Acknowledgments

The authors would like to thank Michael Eggleston, Ryan Going, Tae Joon Seok, and Sangyoon Han for their helpful discussion. This material is based upon work supported under a National Science Foundation Graduate Research Fellowship. This project was also supported by DARPA NACHOS (W911NF-07-1-0314), the NSF Center for Integrated Access Networks (CIAN) (EEC-08120702), the NSF Center for Energy Efficient Electronics Science (E3S) (ECCS-0939514), Samsung GRO (20101554), and the National Research Foundation of Korea Grant funded by the Korean Government (NRF-2010-357-C00041).